Proceedings of ASME Turbo Expo 2020
Turbomachinery Technical Conference and Exposition
GT2020
September 21-25, 2020, Virtual, Online

GT2020-16130

IDENTIFICATION OF HIGH-FREQUENCY TRANSVERSE ACOUSTIC MODES IN MULTI-NOZZLE CAN COMBUSTORS

J. Kim, W. Gillman, D. Wu,
B. Emerson, V. Acharya,
R. Mckinney, T. Lieuwen
Ben T. Zinn Combustion Laboratory
Georgia Institute of Technology
Atlanta, GA, USA

M. Isono, T. Saitoh
Mitsubishi Heavy Industries, Ltd
Takasago-shi, Hyogo, JAPAN

ABSTRACT

High frequency thermoacoustic instabilities are problematic for lean-premixed gas turbines. Identifying which acoustic mode is being excited is important, in that it provides insight into potential mitigation measures and mechanical stress/life. However, the frequency spacing between modes becomes quite close for high frequency instabilities in a can combustor. This makes it difficult to distinguish between the modes (e.g., the first transverse mode vs. a higher order axial/mixed mode) based upon frequency calculations alone, which inevitably have uncertainties in boundary conditions, temperature profiles, and combustion response. This paper presents a methodology to simultaneously identify the acoustic mode shapes in the axial and azimuthal directions from acoustic pressure measurements. Multiple high temperature pressure transducers, located at distinct axial and azimuthal positions, are flush mounted in the combustor wall. The measured pressure oscillations from each sensor are then used to reconstruct the pressure distributions by using a least squares method in conjunction with a solution of a three dimensional wave equation. In order to validate the methodology, finite element method (FEM) calculations with estimated post-flame temperature is used to provide the candidate frequencies and corresponding mode shapes. The results demonstrate the reconstructed mode shapes and standing/spinning character of transverse waves, as well as the associated frequencies, both of which are consistent with the FEM predictions. Nodal line location was also extracted from the experimental data during the instabilities in the pressure data.

NOMENCLATURE

LATIN SYMBOLS

A	Azimuthal amplitude
B	Axial amplitude
c	Sound speed
df	Bandwidth
DR	Direction ratio
F	Fourier transform
f	Frequency
H	Heaviside function
$\mathscr{H}$	Hilbert transform
i	Imaginary unit
J_m	Bessel function of the first kind
k	Axial wave number
L	Spatial matrix in axial direction
l	Radial mode number
M	Spatial matrix in azimuthal direction
m	Azimuthal mode number
$\dot{m}$	mass flow rate
N	Number of grid point
n	Number of sensors
P	Reconstructed pressure matrix
p	Pressure signal
PR	Pilot ratio
R	Combustor radius
$\mathscr{R}$	Air gas constant
R^2	R squares error
r	Radial coordinate
SR	Spin ratio
t	Time
X	Temporal matrix in axial direction
x	Axial coordinate

GREEK SYMBOLS

α_{ml}	Root of dJ_m/dr	θ_n	Nodal line location
γ	Specific heat ratio of air	ϕ	Phasor in azimuthal direction
Θ	Temporal matrix in azimuthal direction	ψ	Phasor in axial direction
θ	Azimuthal coordinate	ω	Angular frequency

OTHERS

$\|\ \|$	Frobenius norm	$\angle$	Phase angle

INTRODUCTION

Lean premixed combustors have significant challenges with self-excited thermoacoustic instabilities. These instabilities occur when unsteady heat release fluctuations constructively interact with the one of the acoustic modes in the combustor, leading to amplitude growth until a limit cycle is reached [1]. Avoiding high amplitude oscillations restricts the operating conditions or, if operating under such conditions, can lead to hardware damage [2].

Thermoacoustic instabilities can occur over a wide range of frequencies and different types of combustors. The particular focus of this paper is on transverse modes. Annular combustors are prone to exhibit low frequency transverse modes [3, 4]. On the other hand, can combustors exhibit high frequency transverse modes referred to as "screech" [5–8]. This screech tone is particularly problematic in combustion industries because its high frequency and high amplitude pressure oscillations damage hardware very rapidly by fatigue failure [9, 10].

Several approaches have been developed to suppress high frequency thermoacoustic instabilities. For example, baffles have been used to modify the acoustic resonance properties and thus dampen the instability in a combustion chamber [11]. In addition, the distribution of propellant injection, porous injector faceplate, and injection geometry have been used to reduce the screech amplitudes [12]. Specifically, acoustic dampers, such as Helmholtz or quarter-wave resonators, are commonly used to suppress high frequency or transverse instabilities as they require physically smaller dampers [13–15]. The performance of these acoustic dampers strongly depends on their location relative to the acoustic mode shapes of the transverse instabilities [16–20]. To efficiently mitigate these transverse instabilities by using acoustic dampers, it is significantly important to identify which acoustic mode is excited.

Different approaches have been used for identifying acoustic mode shapes. For example, Krebs et al. [21], Singla et al. [22] and Bourgouin et al. [23] combined experimental measurements with numerical results to validate a modal analysis. Hale et al. [24] developed a screech wave analysis methodology to differentiate between transverse, longitudinal and complex modes. Poinsot et al. [25, 26], Wolf et al. [27, 28], and Nicoud et al. [29] used a finite element method (FEM) to determine thermoacoustic modes, including unsteady flame effects.

However, most of the approaches previously mentioned have focused on multi-nozzle annular combustors, where the thin gap assumption is applicable, i.e., the length scale of the annular gap is much shorter than that of the combustor's radius. This assumption is not valid for can combustors, where the geometry is not annular, but cylindrical. In addition, can combustors with a large ratio of axial to radial dimension possess multiple transverse and longitudinal modes with natural frequencies that are very close to one another. Because the frequency spacing is very close, it is difficult to distinguish between each mode solely based upon frequency calculations due to the inherent uncertainty in boundary conditions and temperature profiles.

The authors have already proposed a method for reconstructing the mode shape of high frequency instability in [30]. This paper extends and generalizes that work. First, the method in [30] relies on the FEM calculation to estimate sound speed, which is a key parameter to reproduce the mode shape in the axial direction. Thus, the results, such as frequencies and the associated mode shapes, from the experiments and FEM are dependent on each other, which necessarily yields similar results. In contrast, the reconstruction method in the current study removes that dependency so that the FEM can be used to truly provide an independent validation of the method. Second, the data presented in the prior study [30] was so low that the reproduced mode shape was noisy even though the signals were bandpass filtered. However, the intensity in this paper was strong enough that the clear mode shapes had been reproduced. In addition, the two distinct frequencies with narrow spacing were clearly observed, which occurs in a can combustor with a high aspect ratio.

1. EXPERIMENTAL SETUP AND OPERATING CONDITION

Experimental Rig

Figure 1 shows the experimental facility. Air from four inlets enters near the axial midpoint of the rig and flows through an annular section in the upstream direction, cooling the chamber wall. At the front of the test article, the preheated air passes through the eight outer and center pilot nozzles (Fig. 1 (b)) where fuel injectors are located so that the air premixes with methane. The swirl direction of the pilot and outer nozzles are clockwise (CW) and counter-clockwise (CCW), respectively. Fuel flow through the outer and pilot is controlled separately, quantified by the pilot ratio, $PR = \frac{\dot{m}_p}{\dot{m}_p+\dot{m}_o}$ where $\dot{m}_p$ and $\dot{m}_o$ are the fuel flow rate through the pilot and a single outer nozzle, respectively. The combustor liner consists of a metal liner whose diameter and length is 0.29 m and 1.2 m, respectively. The combustor product accelerates near the downstream contraction area and exits the system through the water cooled exhaust.

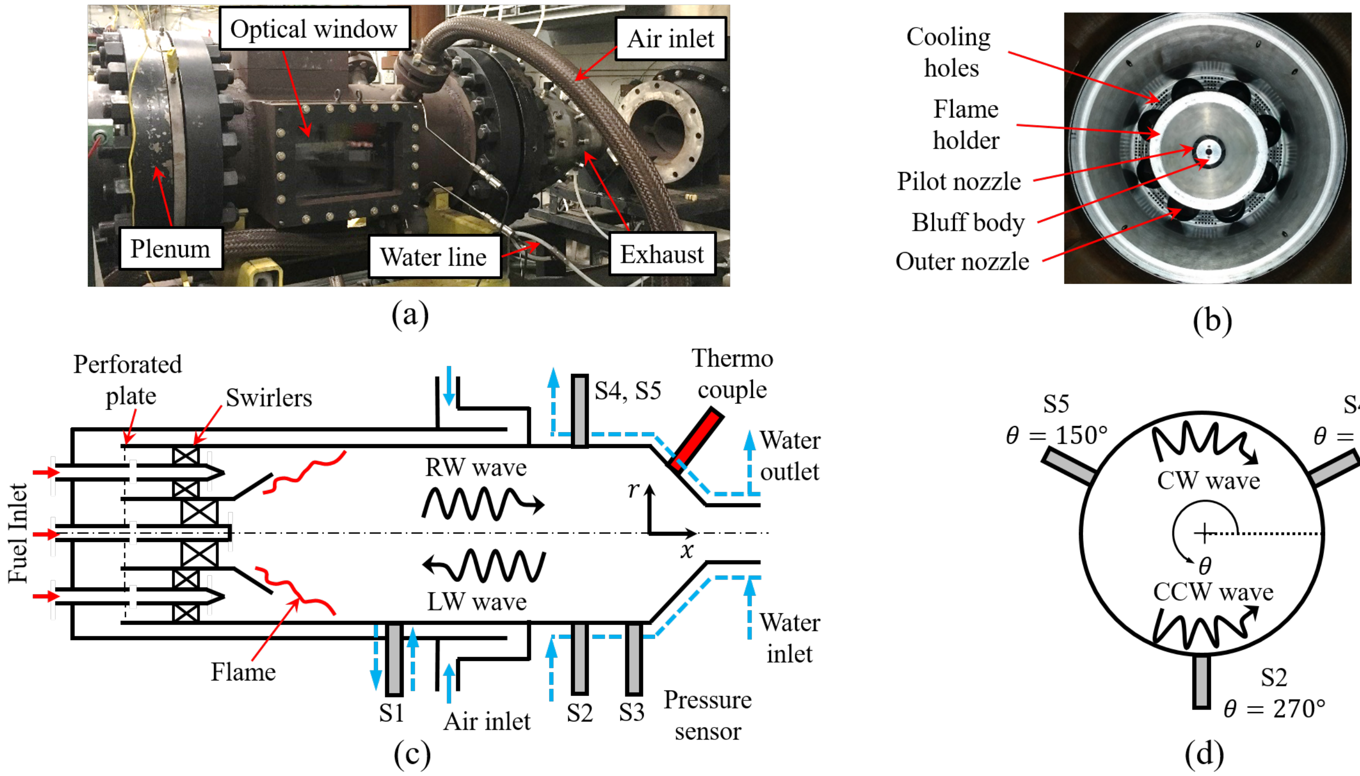

FIGURE 1. EXPERIMENTAL RIG (a) IMAGE OF THE COMBUSTOR (b) IMAGE OF MULTI-NOZZLE (c) SIDE-SCHEMATIC OF THE COMBUSTOR (d) SENSOR CONFIGURATION IN AZIMUTHAL DIRECTION.

Dynamic Pressure Measurement

Five 6021A Kistler pressure sensors (sensitivity: 6200 pC/kPa, range: 10 MPa, accuracy: ±10%) are used to measure the dynamic pressure signals in the post-flame region. Sensors 1-3 are flush mounted at different axial ($x = -0.93, -0.18$, and -0.03 m from the origin in Fig. 1 (c)) but the same azimuthal locations, and sensor 2, 4 and 5 are at different azimuthal, but the same axial locations (Fig. 1 (d)). All sensors are water cooled, and they are connected to a Kistler 5181A differential charge amplifier (sensitivity: 10mV/pC, range: ±10V, accuracy: ±0.2%). A pressure time series is recorded during the entire test run at the sampling frequency of 20 kHz, and then the signals are digitized by a National Instrument (NI 9215) board.

Operating Conditions

Self-excited instabilities occurred at approximately 1600 Hz under a wide range of operating conditions. This paper examines one exemplary test condition, which is summarized in Tab. 1, for acoustic mode identification. At this test condition, two acoustic modes were self-excited during the instabilities.

2. POST PROCESSING

Pressure Data

After recording the data, 1 second of measured signals during the instabilities are extracted for post-processing, which provides approximately 1600 cycles. We explored these same techniques with longer sampling times, but the results changed negligibly. The data at different time sections has been used for repeatability. A time-series pressure signal, given by $p(t)$, is bandpass filtered around each peak frequency, f_p, with a width $df = 60$ Hz to isolate each acoustic mode from the other modes and the broadband noise [31]:

TABLE 1. OPERATING CONDITION DURING TRANSVERSE INSTABILITIES

Preheat temp. (K)	Air flow rate (kg/s)	Equivalence ratio	Pressure (kPa)	Pilot ratio
620	1.474	0.562	190	0.071

$$p'(t) = F^{-1}\Big[F\{p(t)\}\cdot H\Big(f-\Big(f_p-\frac{df}{2}\Big)\Big) \cdot H\Big(-f+\Big(f_p+\frac{df}{2}\Big)\Big)\Big] \quad (1)$$

Here, $p'(t)$ is a filtered pressure signal, F is the Fourier transform, and H is the Heaviside function. The bandwidth is determined such that it is wide enough, but includes only a single peak frequency such that $p'(t)$ contains only one acoustic mode. The filtered signal is then transformed into an analytic signal, $\hat{p}(t)$, by applying Hilbert transform, $\mathscr{H}$ [31]:

$$\hat{p}(t) = p'(t) + \mathscr{H}[p'(t)] \quad (2)$$

This analytic signal is then fitted to the solution of wave equation described in the next section.

General Solution of Wave Equation

In the following development, we assume (i) perfectly cylindrical geometry, (ii) no mean flow due to low Mach number ($M < 0.2$), and (iii) uniform temperature and density after the flame. Then, the solution of the Helmholtz equation of the acoustic wave in a cylindrical duct is given by [1]

$$\hat{p}(x,r,\theta,t) = [A_+e^{im\theta} + A_-e^{-im\theta}] \cdot [B_+e^{ikx} + B_-e^{-ikx}]J_m\Big(\frac{\alpha_{ml}r}{R}\Big)e^{-i\omega t} \quad (3)$$

where $A_\pm$ are slowly time varying amplitudes of CCW(+) and CW(−) waves, $B_\pm$ are slowly time varying amplitudes of right (RW, +) and leftward (LW, −) waves, m is an azimuthal mode number, k is an axial wave number, and ω is the angular frequency. Note that m must be an integer, owing to the periodicity of the azimuthal angle. J_m is the Bessel function of the first kind, R is combustor radius, and l is a radial mode number. α_{ml} is the root of $\frac{d}{dr}J_m(\alpha_{ml}) = 0$. The set of α_{ml} for the different radial and azimuthal mode number is tabulated in Tab. 2.

Here, we would like to clarify terminologies used throughout the paper. When $m = l = 0$, the acoustic mode is "purely" longitudinal where the pressure varies only in the axial direction. Otherwise, the mode is transverse where the pressure varies not only in the axial but also in the azimuthal and radial direction. This transverse mode is classified into azimuthal ($m \neq 0, l = 0$), radial ($m = 0, l \neq 0$), and mixed modes between azimuth and radial ($m \neq 0, l \neq 0$). If the transverse mode has an axial nodal line within the chamber, we call it as a mixed mode between longitudinal and transverse.

TABLE 2. ROOTS OF $\frac{d}{dr}J_m(\alpha_{ml}) = 0$

$\alpha_{ml}/2\pi$	$m=0$	$m=1$	$m=2$	$m=3$
$l=0$	0	0.2930	0.4861	0.6686
$l=1$	0.6098	0.8485	1.0673	1.2757
$l=2$	1.1166	1.3586	1.5867	1.8058

Pressure Reconstruction in Azimuthal Direction

Consider sensors at the same axial and radial, but different azimuthal location. The difference in pressure signals from these sensors is then attributed to only the azimuthal term in Eqn. (3), i.e., the axial and radial terms can be treated as a constant. This constant is set to unity for simplicity, which yields the following model equation in the azimuthal direction.

$$\hat{p}_\theta(\theta,t) = (A_+e^{im\theta} + A_-e^{-im\theta})e^{-i\omega t} \quad (4)$$

Here, the first and the second terms of the right hand side in Eqn. (4) correspond to CCW and CW waves, respectively.

The slowly time varying amplitude can be further decomposed into its magnitude and phasor [32], i.e.

$$\hat{p}_\theta(\theta,t) = (\hat{A}_+e^{i(m\theta+\phi_+)} + \hat{A}_-e^{-i(m\theta-\phi_-)})e^{-i\omega t} \quad (5)$$

where $\hat{A}_\pm$ are positive real valued magnitudes and $\phi_\pm$ are real valued phasors. Given multiple sensor measurements, Eqn. (5) can be rewritten in matrix form:

$$\underbrace{\begin{bmatrix} \hat{p}_\theta(\theta_1,t) \\ \hat{p}_\theta(\theta_2,t) \\ \vdots \\ \hat{p}_\theta(\theta_n,t) \end{bmatrix}}_{P_\theta} = \underbrace{\begin{bmatrix} e^{im\theta_1} & e^{-im\theta_1} \\ e^{im\theta_2} & e^{-im\theta_2} \\ \vdots & \vdots \\ e^{im\theta_n} & e^{-im\theta_n} \end{bmatrix}}_{M} \times \underbrace{\begin{bmatrix} \hat{A}_+e^{i(\phi_+-\omega t)} \\ \hat{A}_-e^{i(\phi_--\omega t)} \end{bmatrix}}_{\Theta} \quad (6)$$

Here, n is the number of sensors and θ_j ($j = 1,2,..,n$) is the azimuthal location of the j^{th} sensor. The matrix, Θ, can then be estimated by using a method of least squares [23], i.e.

$$\Theta = (M^*M)^{-1}M^*P_\theta \quad (7)$$

where M^* is the complex transpose of M. The error of the least squares fit can be quantified by an R squares value, R^2 [22], i.e.

$$\mathrm{R}^2_\theta = 1 - \frac{||P_\theta - M \cdot \Theta||^2}{||P_\theta||^2} \tag{8}$$

where $\|P_\theta\|$ denotes the Frobenius norm of P_θ. Here, $\mathrm{R}^2_\theta = 1$ indicates zero error between the fitting and the experimental data.

The time varying magnitude of each wave is obtained by taking an absolute value of Θ, i.e., $\hat{A}_\pm = |\hat{A}_\pm e^{i(\phi_\pm - \omega t)}|$. Then, the spin ratio, SR, which quantifies the dominant mode between standing and spinning modes, is defined as [23]:

$$SR = \frac{\hat{A}_+ - \hat{A}_-}{\hat{A}_+ + \hat{A}_-} \tag{9}$$

Here, $SR = 0$ indicates a pure standing mode, $SR = \pm 1$ means a pure spinning mode in CCW $(+)$ or CW $(-)$ direction. Otherwise, the mode is a combination of standing and spinning modes.

Furthermore, the pressure distribution in the entire azimuthal direction can be reconstructed by using the matrix, Θ,

$$\underbrace{\begin{bmatrix} \hat{p}_\theta(\theta'_1,t) \\ \hat{p}_\theta(\theta'_2,t) \\ \vdots \\ \hat{p}_\theta(\theta'_N,t) \end{bmatrix}}_{P'_\theta} = \underbrace{\begin{bmatrix} e^{i\theta'_1} & e^{-im\theta'_1} \\ e^{i\theta'_2} & e^{-im\theta'_2} \\ \vdots & \vdots \\ e^{i\theta'_N} & e^{-im\theta'_N} \end{bmatrix}}_{M'} \times \Theta \tag{10}$$

where θ'_j $(j = 1,2,..,N)$ is the azimuthal position ranging from 0 to 2π, and N is the number of grid points. Given the complex spatio-temporal pressure matrix, P'_θ, one can plot the magnitude and phase distributions along the azimuthal direction at each realization. However, the actual distributions significantly vary in time, which hinders identification of the mode shape. Thus, to minimize the variation of the distributions,

1. The magnitude distribution at each realization is normalized by its spatial average.
2. The phase distribution at each realization is plotted with respect to one of the sensors.
3. Then, the temporal averaged of both distributions with the error bar are plotted to visualize the mode shape.

Last, the nodal line position, given by θ_n, is defined as the location where the pressure magnitude is minimum. Given that the azimuthal distribution of the pressure can be written as a superposition of a standing and spinning wave, this definition necessarily locates the nodal line of the standing wave portion. Moreover, it becomes meaningless for a pure spinning wave. This nodal line location can be calculated by taking the partial derivative of $|\hat{p}_\theta(\theta,t)|^2$ with respect to θ.

$$\theta_n(t) = \frac{j\pi - (\phi_+ - \phi_-)}{2m}, \text{ where } j = 1,3,5.. \tag{11}$$

The right hand side in Eqn. (11) is evaluated by subtracting the angle of each wave in matrix, Θ, i.e.,$\phi_\pm - \omega t = \angle(\hat{A}_\pm e^{i(\phi_\pm - \omega t)})$. Then, the pressure magnitude square is rewritten as:

$$|\hat{p}_\theta(\theta)|^2 = \hat{A}^2_+ + \hat{A}^2_- + 2\hat{A}_+\hat{A}_- \cos(2m(\theta - \theta_n) + j\pi) \tag{12}$$

Equation (12) explicitly shows that the pressure magnitude at a given sensor location depends on both the wave amplitudes, $\hat{A}_\pm$, and the location of the nodal line. Specifically, the effect of the nodal line position on the pressure magnitude is maximized when $\hat{A}_+ = \hat{A}_-$(or standing mode). In this case, the magnitude is zero at the nodal line $(\theta = \theta_n)$, and maximum at the anti-nodal line $(\theta = \theta_n \pm \pi/2m)$. This magnitude dependency on the nodal line diminishes as the $\hat{A}_+\hat{A}_-$ product gets smaller, such as when the mode converges to a spinning mode, i.e., $\hat{A}_+ = 0$ or $\hat{A}_- = 0$. In this case, the magnitude is constant regardless of the sensor position, and the nodal line cannot be defined. Therefore, considering the uncertainty of the data, the nodal line is defined only when $|SR| < 0.9$.

Pressure Reconstruction in Axial Direction

Similarly, considering sensors at the same radial and azimuthal, but different axial locations, the acoustic wave in the axial direction can be modeled as a combination of RW and LW waves with time dependent magnitudes and phasors, i.e.

$$\hat{p}_x(x,t) = (\hat{B}_+ e^{i(kx+\psi_+)} + \hat{B}_- e^{-i(kx-\psi_-)})e^{-i\omega t} \tag{13}$$

where $\hat{B}_\pm$ and $\hat{\psi}_\pm$ are magnitudes and phasors of RW $(+)$ and LW $(-)$ waves, respectively. Given multiple sensor measurements at the same radial and azimuthal, but different axial locations, Eqn. (13) can be rewritten as a matrix form, i.e.

$$\underbrace{\begin{bmatrix} \hat{p}_x(x_1,t) \\ \hat{p}_x(x_2,t) \\ \vdots \\ \hat{p}_x(x_n,t) \end{bmatrix}}_{P_x} = \underbrace{\begin{bmatrix} e^{ikx_1} & e^{-ikx_1} \\ e^{ikx_2} & e^{-ikx_2} \\ \vdots & \vdots \\ e^{ikx_n} & e^{-ikx_n} \end{bmatrix}}_{L} \times \underbrace{\begin{bmatrix} \hat{B}_+ e^{i(\psi_+ - \omega t)} \\ \hat{B}_- e^{i(\psi_- - \omega t)} \end{bmatrix}}_{X} \tag{14}$$

where x_j $(j = 1,2,..,n)$ denotes the axial location of j^{th} sensor. It should be noted that, unlike the azimuthal mode number, the axial wave number is not necessarily an integer. Therefore, it must be evaluated in advance to apply a least squares method. This paper estimates the axial wave number that minimizes a least squares error, using a procedure detailed in the Appendix. Once the axial wave number is obtained, the matrix, X, can be estimated by a least squares fit.

$$X = (L^*L)^{-1}L^*P_x \tag{15}$$

The error of the fitting is given by

$$\mathrm{R}_x^2 = 1 - \frac{||P_x - L\cdot X||^2}{||P_x||^2}. \tag{16}$$

The direction ratio is then defined as

$$DR = \frac{\hat{B}_+ - \hat{B}_-}{\hat{B}_+ + \hat{B}_-} \tag{17}$$

Here, $DR = 0$ indicates a pure standing mode, and $DR = \pm 1$ means pure RW (+) and LW (–) traveling modes. Otherwise, it is a combination of standing and traveling modes. The axial pressure distribution can then be reproduced as follows:

$$\underbrace{\begin{bmatrix} \hat{p}_x(x'_1,t) \\ \hat{p}_x(x'_2,t) \\ \vdots \\ \hat{p}_x(x'_N,t) \end{bmatrix}}_{P'_x} = \underbrace{\begin{bmatrix} e^{ikx'_1} & e^{-ikx'_1} \\ e^{ikx'_2} & e^{-ikx'_2} \\ \vdots & \vdots \\ e^{ikx'_N} & e^{-ikx'_N} \end{bmatrix}}_{L'} \times X \tag{18}$$

where $x'_j (j = 1,2,..,N)$ is an axial coordinate. By plotting the pressure in the axial direction, one can visualize the axial mode shape. Notice that this reconstruction method is not applicable across the flame or the contraction area due to assumptions (i) and (iii).

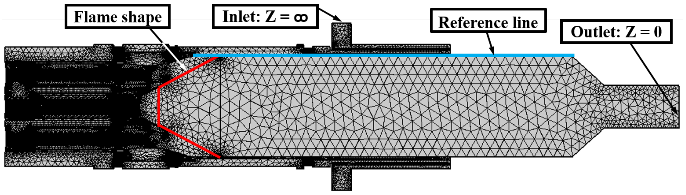

FIGURE 2. MESH, BOUNDARY CONDITIONS, AND FLAME SHAPE.

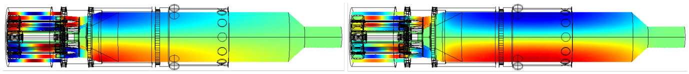

(a) 1T-a mode

(b) 1T-b mode

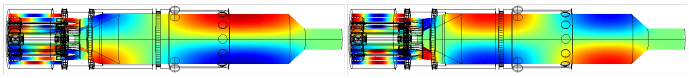

(c) 1L1T-a mode

(d) 1L1T-b mode

FIGURE 3. TRANSVERSE ACOUSTIC MODE SHAPES OBTAINED FROM FEM. 'L' AND 'T' STAND FOR LONGITUDINAL AND TRANSVERSE, RESPECTIVELY.

3. COMPUTATIONAL ANALYSIS

The FEM solver COMSOL Multiphysics is used to calculate the acoustic mode shapes at the experimental conditions. Figure 2 shows a two-dimensional slice of the entire computational domain. The acoustic boundary condition for the inlet is set to rigid because of the choked orifices, and the outlet to pressure release. All other solid surfaces including walls are regarded as a rigid boundary with infinite impedance. The flame is regarded as a cone shape, and the temperature of the domains before and after the flame is set to uniform with preheat and combustion temperature, respectively. The detail description of estimation of combustion temperature is illustrated in the Appendix. The computational domain is meshed with 2,495,747 tetrahedral elements, which gives 3,811,121 of degrees of freedom to be resolved. The FEM is then carried out to solve the Helmholtz equation to predict eigenfrequencies and the corresponding mode shapes. Based upon the frequencies observed from the experiments, this study considers only the first four transverse modes, which are shown in Fig. 3. It was found that the boundary conditions at the outlet have a negligible effect on the eigenfrequencies and the associated mode shapes. This is because the cutoff frequency drops at the area contraction, thus, the wave magnitude exponentially decays in axial direction, preventing it from interacting with the outlet boundary.

4. RESULTS

Frequency Spectrum

Figure 4 shows the frequency spectrum measured from sensor 1 and 3 for 1s during the instabilities. The peak frequency

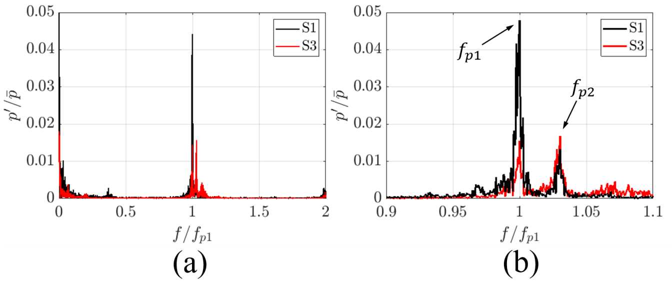

(a) (b)

FIGURE 4. MEASURED FREQUENCY SPECTRUM FROM SENSOR 1 AND 3. (a) ZOOM OUT (b) ZOOM IN. FREQUENCY AND PRESSURE AMPLITUDE ARE NORMALIZED BY ITS PEAK FREQUENCY AND STATIC PRESSURE, RESPECTIVELY.

of the instability was around 1600 Hz. The rough calculation from the FEM provides that the frequencies of the second azimuthal ($m = 2$) and the first radial ($l = 1$) modes occur at approximately 2700 and 3500 Hz, respectively, which are much greater than the observed frequencies. This confirms that the instabilities are either a pure longitudinal ($m = 0, l = 0$) or azimuthal mode ($m = 1, l = 0$).

Notice that two distinct peaks appeared in the spectrum, the first peak at $f_{p1}/f_{p1} = 1$ and the second at $f_{p2}/f_{p1} = 1.03$, illustrating these closely spaced natural frequencies. The acoustic mode identification is carried out for each peak.

Acoustic Mode Identification

This section describes the pressure dynamics and the acoustic mode shapes during the instabilities. We will investigate the azimuthal and axial dependency separately.

Azimuthal Dependency. Figure 5 (a) shows the pressure signals from each sensor filtered at $f_{p1} \pm df/2$. Notice that the magnitudes (or envelopes) of each signal are similar to each other, but the phases are different. This observation clearly indicates that the instability is not only the first azimuthal mode ($m = 1$) but also close to a spinning mode. CCW and CW waves are extracted by using a least squares fit given by Eqn. (7). Then, the spin ratio and the nodal line are evaluated and plotted in Fig. 5 (c) and (e). The spin ratio is close to unity indicating that the mode is CCW dominant.

In Fig. 5 (e), the nodal line hovers at around $-10°$ and it jumps in CCW direction at $t = 0.4$s to around $170°$. The similar behavior is observed at $t = 0.05$s, but in this case, the nodal line jumps in the other direction. This behavior seems to occur at the spin ratio near unity. The possible explanation for this phenomenon is that when the mode becomes an instantaneously pure spinning mode, the nodal line disappears, and when the mode comes back to a mixed mode, the nodal line reappears. This re-established nodal line may now be located at completely different locations from the initial location, which appears to be a nodal line jumping. The similar explanation is described in [33]. In addition, bearing in mind that the nodal line is straight, the line at $-10°$ is the same at $170°$, which implies that the nodal line seems to hover at a fixed location. This may be attributed to the non-uniformity of the temperature or flow field in azimuthal direction. Lastly, the nodal line is closest to sensor 5 and furthest from sensor 2, yielding the minimum magnitude at sensor 5 and maximum magnitude at sensor 2 in Fig. 5 (a). As mentioned before, however, the magnitude difference is small because of the nearly spinning mode.

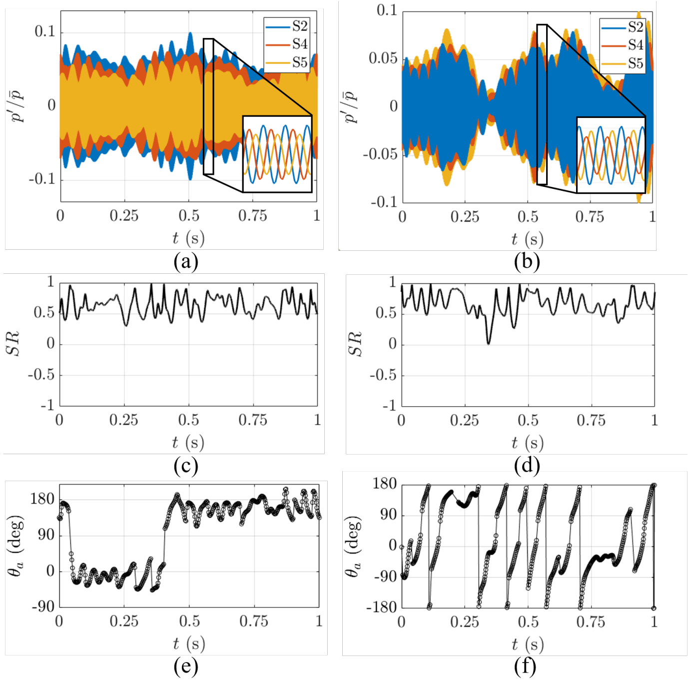

(a) (b) (c) (d) (e) (f)

FIGURE 5. MEASURED PRESSURE SIGNALS IN TIME SERIES FILTERED AT (a) $f_{p1} \pm df/2$ AND (b) $f_{p2} \pm df/2$. THE PRESSURE IS NORMALIZED BY STATIC PRESSURE. SPIN RATIO ((c) f_{p1}, (d) f_{p2}) AND NODAL LINE ((e) f_{p1}, (f) f_{p2}) IN TIME SERIES.

Figure 5 (b) shows the pressure signals filtered at $f_{p2} \pm df/2$. Notice that the pressure magnitudes are also similar to each other, implying that the mode is close to the spinning mode. This is obvious in the spin ratio plot in Fig. 5 (d) where the spin ratio is close to unity. However, unlike f_{p1}, the nodal line is predominantly rotating in CCW direction.

The pressure magnitude and phase distributions along the azimuthal direction are reconstructed by Eqn. (10) and plotted in Fig. 6. Here, the black solid line is the temporal averaged pressure distribution and the dashed lines denote the standard error. The red cross represents the temporal averaged magnitude or the

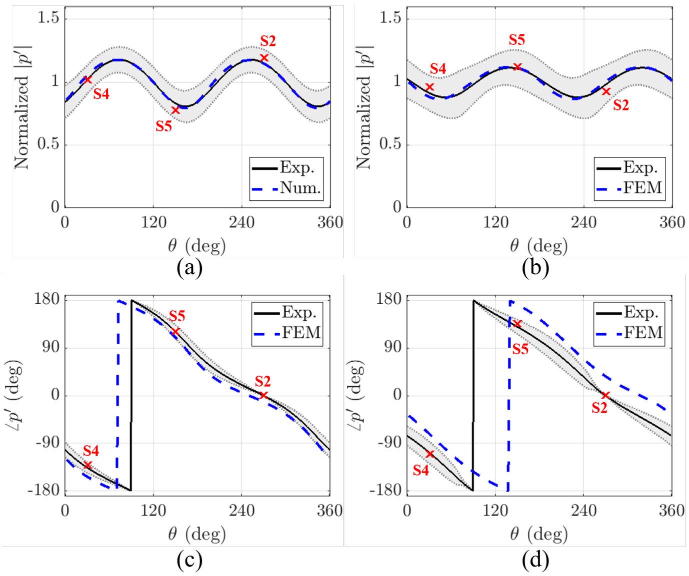

FIGURE 6. PRESSURE MAGNITUDE ALONG THE AZIMUTHAL DIRECTION: (a) f_{p1} (b) f_{p2}. THE MAGNITUDE IS NORMALIZED BY ITS SPATIAL AVERAGED VALUE. PRESSURE PHASE ALONG THE AZIMUTHAL DIRECTION: (c) f_{p1} (d) f_{p2}. THE PHASE IS PLOTTED WITH RESPECT TO SENSOR 2.

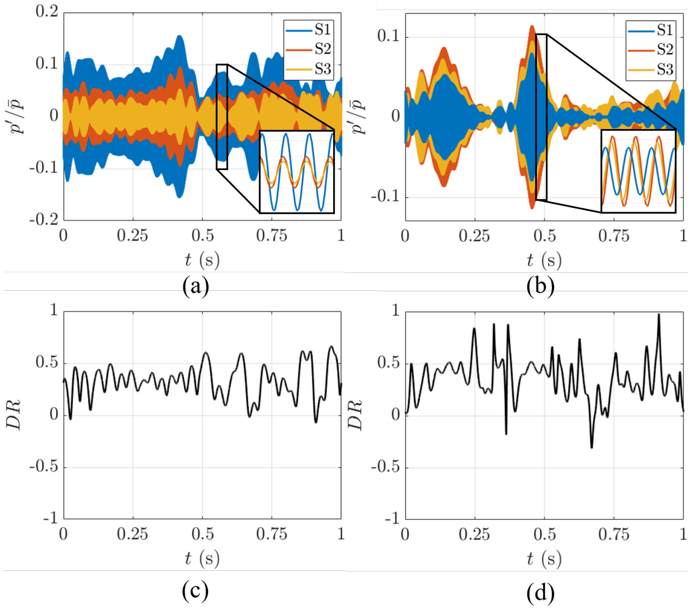

FIGURE 7. MEASURED PRESSURE SIGNALS IN TIME SERIES FILTERED AT (a) $f_{p1} \pm df/2$ AND (b) $f_{p2} \pm df/2$. THE PRESSURE IS NORMALIZED BY STATIC PRESSURE. DIRECTION RATIO IN TIME SERIES: (c) f_{p1} (d) f_{p2}.

phase from each sensor. The blue dash line denotes the distribution for 1T-a (Fig. 6 (a), (c)) and 1L1T-a (Fig. 6 (b), (d)) modes from the FEM results in Fig. 3. The axial location in FEM is selected at the same axial position of sensor 2.

In Fig. 6 (a), the pressure magnitude of f_{p1} varies in the azimuthal direction, indicating that it is not a pure longitudinal, but an azimuthal mode. In addition, non-zero magnitude at the nodal line implies that the mode is not standing, but rather close to the spinning mode. Last, the phase distribution from the experiments in Fig. 6 (c) shows almost linear relationship with θ, which is the characteristic of the spinning mode.

It should be emphasized that the FEM, which solves the Helmholtz equation, provides two orthogonal standing mode solutions. The actual mode is then a linear combination of two solutions. For example, if either of two solutions is negligible, then the resultant mode is pure standing, whereas if the two solutions are equally dominant, the resultant mode is pure spinning. In real combustors, however, the dominance of each solution depends on the test conditions, providing standing, spinning or a combination of both modes [33–36]. In Fig. 6, the two orthogonal solutions are linearly combined such that the resultant mode is similar to those from the experiments.

Figure 6 (b) and (d) also shows a spinning mode shape, but the detail description is omitted here as the general features are similar to those in Fig. 6 (a) and (c).

Axial Dependency. Even though we found the instabilities to be the first azimuthal modes, they may also have an axial dependency. Given the frequency and the estimated sound speed, the axial wave number for f_{p1} was found to be purely imaginary, implying that the pressure magnitude exponentially decays in the axial direction. This evanescent wave occurs due to a temperature jump across the flame [37]. This feature is evident in the pressure magnitude distribution in Fig. 8 (a).

Figure 7 (a) and (b) describe the pressure signals filtered at $f_{p1} \pm df/2$ and $f_{p2} \pm df/2$, respectively. In Fig. 7 (a), the pressure magnitude is maximum for sensor 1 and minimum for sensor 3, whereas in Fig. 7 (b), the magnitude is maximum for sensor 2 and minimum for sensor 1. Figure 7 (c) and (d) show that the direction ratios for both peaks fluctuate at a positive value, implying that the mode is slightly propagating in the RW direction. For f_{p1}, however, recall that the axial wave number is imaginary, yielding the magnitude in RW and LW direction to be $\hat{B}_{\pm}e^{\mp k_i x}$ where $k_i = k/i$; i.e., the magnitude depends on the axial position as well as $\hat{B}_{\pm}$. In other words, the acoustic wave generated by the flame propagates in the RW direction, but the magnitude of the RW wave exponentially decays, which then leads to an extremely small magnitude in the LW wave at the reflection boundary. Therefore, the magnitude of the LW wave would be negligible compared to that of the RW wave, leading to a nearly traveling wave in RW direction. The reason for the direction ratio far from the unity in Fig. 7 (c) is that Eqn. (17) does not

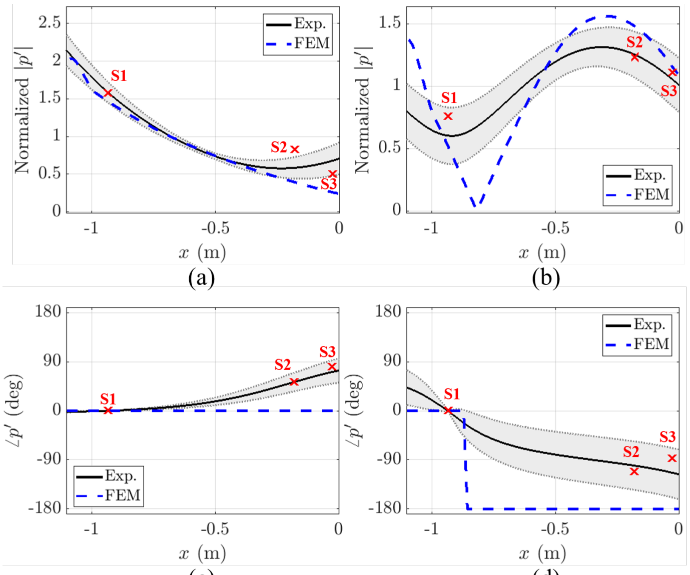

(a) (b)

(c) (d)

FIGURE 8. PRESSURE MAGNITUDE ALONG THE AXIAL DIRECTION: (a) f_{p1} (b) f_{p2}. PRESSURE PHASE ALONG THE AXIAL DIRECTION: (c) f_{p1} (d) f_{p2}. THE PHASE IS PLOTTED WITH RESPECT TO SENSOR 1.

account for the axial dependent term, $e^{\mp k_i x}$, when the axial wave number is imaginary.

Figure 8 presents the pressure magnitude and the phase distributions along the reference line indicated in Fig. 2. Here, $x = 0$ corresponds to the axial location at the area contraction in the combustor. The FEM is plotted for 1T-a (Fig. 8 (a), (c)) and 1L1T-a (Fig. 8 (b), (d)) modes from Fig. 3. In Fig. 8 (a) and (c), notice that FEM also predicts the evanescent wave for f_{p1}. However, the discrepancy between the experiments and the FEM appears at the right end of the domain. This difference originates from the fact that for evanescent wave, FEM predicts only the RW wave, resulting in a monotonically decreasing magnitude and constant phase, whereas the reconstruction method takes into account both RW and LW waves in Eqn. (13). Whether to include the LW wave or not is indeterminate, but without the LW wave, the phase variation between the sensors in Fig. 8 (c) would not be explained. Except for this deviation, the magnitude and the phase from the experiments are in good agreement with those from the FEM. For f_{p2} in Fig. 8 (b) and (d), the experimental data shows the slightly RW propagating mode, whereas the FEM predicts the perfect standing mode. This may be attributed to the effect of mean flow [1] or the boundary condition at the outlet,. i.e., some of the acoustic energy leaves the domain through the exhaust. However, considering the nodal line location in Fig. 8 (b) and phase variation in Fig. 8 (d), the experimental data is close to the FEM results.

TABLE 3. R^2 VALUES AND COMPARISON BETWEEN EXPERIMENTAL AND FEM RESULTS.

Frequency	Mode	$\Delta f / f_{\mathrm{FEM}}$ (%)	R^2	
f_{p1}	1T-a	0.139	R^2_θ	0.9961
			R^2_x	0.9543
f_{p2}	1L1T-a	0.422	R^2_θ	0.9940
			R^2_x	0.8912

To sum up the acoustic mode shapes, we can conclude that f_{p1} and f_{p2} correspond to 1T-a and 1L1T-a modes, respectively, which are described in Fig. 3 (a) and (c) from the FEM results. The R^2 values of each direction and the frequency comparison between the experimental and the FEM results are summarized in Tab. 3. Here, $\Delta f = |f_{\mathrm{exp}} - f_{\mathrm{FEM}}|$.

5. CONCLUSION

In this study, the acoustic mode shapes of transverse instabilities in a multi-nozzle can combustor have been investigated. During these instabilities, two strong distinct peaks were observed, which is a common observation in a can combustor with a longer axial than radial dimension. The rough calculation from the FEM suggests that the observed frequencies were either a pure longitudinal or azimuthal mode. Then, the different pressure signals between the sensors at distinct azimuthal locations confirm that the instabilities correspond to the first azimuthal modes. However, the axial dependency of each mode is difficult to be identified solely from the FEM as the eigenfrequencies of each mode are too close to each other, which motivates the current study.

This paper has introduced the methodology to reconstruct the pressure distributions in axial and azimuthal direction by using measured signals from multiple pressure sensors as well as the solution of the wave equation in a cylindrical cavity. The results from the reconstruction method are compared with those from the FEM to validate the method. For the azimuthal distribution, both peaks indicated that the modes are close to a spinning wave. The axial distribution for the first peak showed evanescent wave, and, for the second peak, it manifested propagating wave. These distributions show a good agreement between the experiments and the FEM results, validating the first and the second peaks as 1T-a and 1L1T-a modes, respectively. In conclusion, the methodology presented in this paper can be used to identify the high frequency transverse acoustic modes even though their frequencies are close to each other.

ACKNOWLEDGMENT

This study has been partially supported by Mitsubishi Heavy Industry. The authors gratefully acknowledge the support of the University Turbine Systems Research (contract #DE-FE0031285) program under contract monitor Dr. Mark Freeman.

REFERENCES

[1] Lieuwen, T. C., 2012. *Unsteady combustor physics*. Cambridge University Press, Cambridge, U.K.

[2] Lieuwen, T. C., and Yang, V., 2005. *Combustion instabilities in gas turbine engines: operational experience, fundamental mechanisms, and modeling*, Vol. 210. American Institute of Aeronautics and Astronautics, Reston, VA.

[3] Krebs, W., Bethke, S., Lepers, J., Flohr, P., Prade, B., Johnson, C., and Sattinger, S., 2005. "Thermoacoustic design tools and passive control: Siemens power generation approaches". *Combustion Instabilities in Gas Turbine Engines Operational Experience, Fundamental Mechanisms and Modeling*.

[4] Zellhuber, M., Meraner, C., Kulkarni, R., Polifke, W., and Schuermans, B., 2013. "Large eddy simulation of flame response to transverse acoustic excitation in a model reheat combustor". *Journal of Engineering for Gas Turbines and Power,* ***135***(9), p. 091508.

[5] Rogers, D. E., 1956. "A mechanism for high-frequency oscillation in ramjet combustors and afterburners". *Journal of Jet Propulsion,* ***26***(6), pp. 456–462.

[6] Elias, I., 1959. "Acoustical resonances produced by combustion of a fuel-air mixture in a rectangular duct". *The Journal of the Acoustical Society of America,* ***31***(3), pp. 296–304.

[7] Kaskan, W., and Noreen, A., 1955. "High-frequency oscillations of a flame held by a bluff body". *ASME Transactions,* ***77***(6), pp. 855–891.

[8] Ebrahimi, H. "Overview of gas turbine augmentor design, operation, and combustion oscillation". In 42nd AIAA/ASME/SAE/ASEE Joint Propulsion Conference & Exhibit, p. 4916.

[9] Sewell, J. B., and Sobieski, P. A., 2005. "Monitoring of combustion instabilities: Calpine's experience". *Combustion Instabilities in Gas Turbine Engines: Operational Experience, Fundamental Mechanisms, and Modeling,* ***210***, pp. 147–162.

[10] Harp, J. L., Velie, W. W., and Bryant, L., 1954. *Investigation of Combustion Screech and a Method of its Control*. National Advisory Committee for Aeronautics.

[11] Laudien, E., Pongratz, R., Pierro, R., and Preclik, D., 1995. "Experimental procedures aiding the design of acoustic cavities". *Liquid Rocket Engine Combustion Instability,* ***169***, pp. 377–399.

[12] Wanhainen, J. P., Hannum, N. P., and Russell, L. M., 1967. *Evaluation of Speech Suppression Concepts in a 20,000 Pound Thrust Hydrogen Oxygen Rocket*. National Aeronautics and Space Administration.

[13] Vincent, D. W., 1968. *Experimental Investigation of Acoustic Liners to Suppress Screech in Storable Propellant Rocket Motors*. National Aeronautics and Space Administration.

[14] Harrje, D. T., 1972. *Liquid propellant rocket combustion instability*, Vol. 194. Scientific and Technical Information Office, National Aeronautics and Space Administration.

[15] Garrison, G. "The role of acoustic absorbers in preventing combustion instability". In 7th Propulsion Joint Specialist Conference, p. 699.

[16] Stow, S. R., and Dowling, A. P. "Modelling of circumferential modal coupling due to helmholtz resonators". In ASME Turbo Expo 2003, collocated with the 2003 International Joint Power Generation Conference, American Society of Mechanical Engineers Digital Collection, pp. 129–137.

[17] Camporeale, S., Forte, A., Fortunato, B., Mastrovito, M., and Ferrante, A. "Numerical simulation of the acoustic pressure field in an annular combustion chamber with helmholtz resonators". In ASME Turbo Expo 2004: Power for Land, Sea, and Air, American Society of Mechanical Engineers Digital Collection, pp. 713–724.

[18] Zahn, M., Schulze, M., Hirsch, C., and Sattelmayer, T. "Impact of quarter wave tube arrangement on damping of azimuthal modes". In ASME Turbo Expo 2016: Turbomachinery Technical Conference and Exposition, American Society of Mechanical Engineers Digital Collection.

[19] Betz, M., Wagner, M., Zahn, M., Stadlmair, N. V., Schulze, M., Hirsch, C., and Sattelmayer, T. "Impact of damper parameters on the stability margin of an annular combustor test rig". In ASME Turbo Expo 2017: Turbomachinery Technical Conference and Exposition, American Society of Mechanical Engineers Digital Collection.

[20] Mazur, M., Nygård, H. T., Dawson, J., and Worth, N. "Experimental study of damper position on instabilities in an annular combustor". In ASME Turbo Expo 2018: Turbomachinery Technical Conference and Exposition, American Society of Mechanical Engineers Digital Collection.

[21] Krebs, W., Walz, G., Flohr, P., and Hoffmann, S. "Modal analysis of annular combustors: Effect of burner impedance". In ASME Turbo Expo 2001: Power for Land, Sea, and Air, American Society of Mechanical Engineers, pp. V002T02A009–V002T02A009.

[22] Singla, G., Noiray, N., and Schuermans, B. "Combustion dynamics validation of an annular reheat combustor". In ASME Turbo Expo 2012: Turbine Technical Conference and Exposition, American Society of Mechanical Engineers Digital Collection, pp. 447–455.

[23] Bourgouin, J.-F., Durox, D., Moeck, J. P., Schuller, T., and Candel, S. "Self-sustained instabilities in an annular

combustor coupled by azimuthal and longitudinal acoustic modes". In ASME Turbo Expo 2013: Turbine Technical Conference and Exposition, American Society of Mechanical Engineers Digital Collection.

[24] Hale, A. A., Cothran, W. D., and Sabo, K. M. "Analysis technique to determine the underlying wave structure of combustion instabilities from surface mounted high response static pressure sensors". In ASME Turbo Expo 2018: Turbomachinery Technical Conference and Exposition, American Society of Mechanical Engineers Digital Collection.

[25] Staffelbach, G., Gicquel, L., Boudier, G., and Poinsot, T., 2009. "Large eddy simulation of self excited azimuthal modes in annular combustors". *Proceedings of the Combustion Institute,* ***32***(2), pp. 2909–2916.

[26] Poinsot, T., Wolf, P., Staffelbach, G., Gicquel, L., and Muller, J., 2011. "Identification of azimuthal modes in annular combustion chambers". *Center for Turbulence Research Annual Research Briefs,* ***2011***, pp. 249–258.

[27] Wolf, P., Staffelbach, G., Roux, A., Gicquel, L., Poinsot, T., and Moureau, V., 2009. "Massively parallel les of azimuthal thermo-acoustic instabilities in annular gas turbines". *Comptes Rendus Mecanique,* ***337***(6-7), pp. 385–394.

[28] Wolf, P., Staffelbach, G., Gicquel, L. Y., Müller, J.-D., and Poinsot, T., 2012. "Acoustic and large eddy simulation studies of azimuthal modes in annular combustion chambers". *Combustion and Flame,* ***159***(11), pp. 3398–3413.

[29] Nicoud, F., Benoit, L., Sensiau, C., and Poinsot, T., 2007. "Acoustic modes in combustors with complex impedances and multidimensional active flames". *AIAA journal,* ***45***(2), pp. 426–441.

[30] Kim, J., Lieuwen, T., Emerson, B., Acharya, V., Wu, D., Mckinney, R., Wang, X., and Isono, M. "High-frequency acoustic mode identification of unstable combustors". In ASME Turbo Expo 2019: Turbomachinery Technical Conference and Exposition, American Society of Mechanical Engineers Digital Collection.

[31] Berger, F. M., Hummel, T., Hertweck, M., Kaufmann, J., Schuermans, B., and Sattelmayer, T., 2017. "High-frequency thermoacoustic modulation mechanisms in swirl-stabilized gas turbine combustors—part i: Experimental investigation of local flame response". *Journal of Engineering for Gas Turbines and Power,* ***139***(7), p. 071501.

[32] Hummel, T., Berger, F., Schuermans, B., and Sattelmayer, T., 2016. "Theory and modeling of non-degenerate transversal thermoacoustic limit cycle oscillations". *GTRE-038*.

[33] Dawson, J. R., and Worth, N. A., 2014. "Flame dynamics and unsteady heat release rate of self-excited azimuthal modes in an annular combustor". *Combustion and Flame,* ***161***(10), pp. 2565–2578.

[34] Mazur, M., Nygård, H. T., Dawson, J. R., and Worth, N. A., 2019. "Characteristics of self-excited spinning azimuthal modes in an annular combustor with turbulent premixed bluff-body flames". *Proceedings of the Combustion Institute,* ***37***(4), pp. 5129–5136.

[35] Worth, N. A., and Dawson, J. R., 2017. "Effect of equivalence ratio on the modal dynamics of azimuthal combustion instabilities". *Proceedings of the Combustion Institute,* ***36***(3), pp. 3743–3751.

[36] Worth, N. A., and Dawson, J. R., 2013. "Modal dynamics of self-excited azimuthal instabilities in an annular combustion chamber". *Combustion and Flame,* ***160***(11), pp. 2476–2489.

[37] Schulze, M., Hummel, T., Klarmann, N., Berger, F., Schuermans, B., and Sattelmayer, T., 2017. "Linearized euler equations for the prediction of linear high-frequency stability in gas turbine combustors". *Journal of Engineering for Gas Turbines and Power,* ***139***(3), p. 031510.

Appendix: Sound Speed Estimation

In order to utilize Eqn. (15), we must determine the axial wave number in advance, which depends on the sound speed. The axial wave number and the sound speed are related by the dispersion relation. For homogeneous sound speed with no mean flow in a cylindrical cavity, the dispersion relation is given by [1]

$$f = \frac{c}{2\pi}\sqrt{\left(\frac{\alpha_{ml}}{R}\right)^2 + k^2} \tag{19}$$

where c is sound speed. Given the frequency spectrum in Fig. 4 and the dispersion relation, we can reduce the number of unknowns to one, which is sound speed in this case.

Without any noise, R_x^2 given by Eqn. (16) would be unity. However, the noise is inevitable in a turbulent combustion environment, resulting in R_x^2 less than unity. Therefore, R_x^2 is evaluated for a range of values of sound speed, and the optimal sound speed is determined as the value that maximizes R_x^2 [22].

$$c_{\mathrm{opt}} = \underset{c\in[c_l,c_u]}{\operatorname{argmax}} \mathrm{R}_x^2 \tag{20}$$

where $c_{l/u}$ are the lower and the upper bounds for the sound speed values, which are estimated from the measured temperature at the exhaust (1200 K) and the adiabatic flame temperature (1800 K), respectively. R_x^2 was evaluated at the range of sound speed given each peak, f_{p1} and f_{p2}, yielding two plots of R_x^2 with respect to sound speed values as shown in Fig. 9. Here, $\mathrm{R}_{x,1}^2$

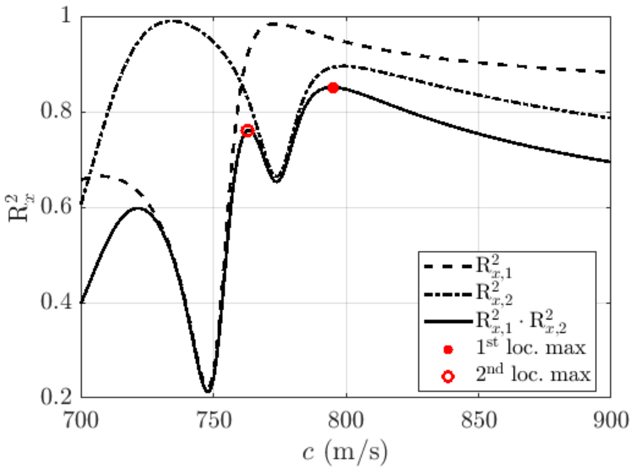

FIGURE 9. R_x^2 WITH RESPECT TO SOUND SPEED FOR EACH PEAK.

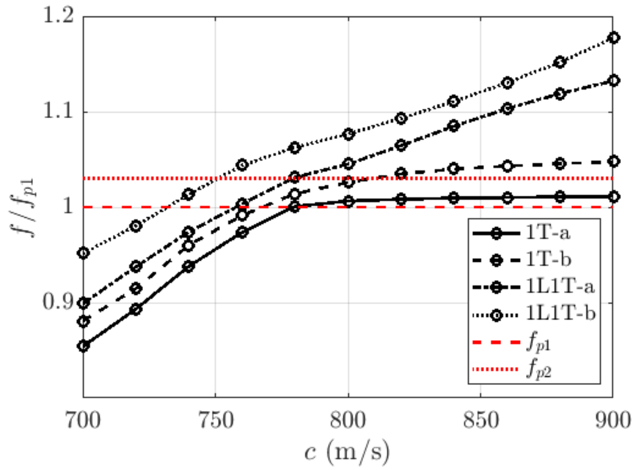

FIGURE 10. SOUND SPEED VERSUS EIGENFREQUENCY OF EACH MODE OBTAINED FROM FEM.

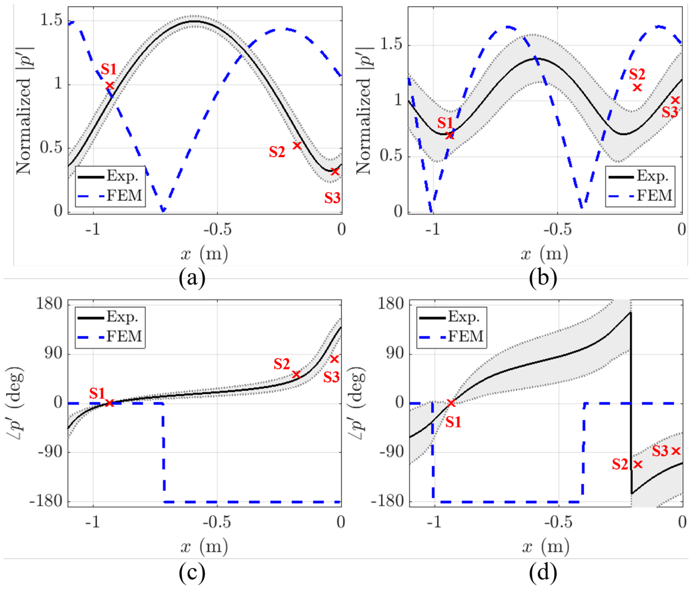

FIGURE 11. PRESSURE MAGNITUDE AND PHASE DISTRIBUTIONS ALONG THE AXIAL DIRECTION FOR $c = 763$ m/s. (a), (c): 1L1T-a MODE. (b), (d): 1L1T-b MODE.

and $\mathrm{R}_{x,2}^2$ denote the R_x^2 value of f_{p1} and f_{p2}, respectively. The optimal sound speed is supposed to maximize each R_x^2 simultaneously, but the trends of each R_x^2 are quite different. Therefore, the optimal value is selected such that it maximizes the product of each R_x^2 or $\mathrm{R}_{x,1}^2 \cdot \mathrm{R}_{x,2}^2$. In Fig. 9, the two red dots represent the first and the second local maxima of $\mathrm{R}_{x,1}^2 \cdot \mathrm{R}_{x,2}^2$. As shown in the result section, the sound speed of the first maxima, which is 794 m/s, shows a good agreement with the results from the FEM, validating the method of sound speed estimation. For reference, this sound speed value corresponds to a temperature of 1570 K. However, considering the uncertainty of the least squares fit, the value at the other local maxima, which is 763 m/s, is also investigated here.

Figure 10 illustrates the eigenfrequencies of each mode obtained from the FEM depending on the sound speed at the combustion region. Note that the eigenfrequencies of 1T-a and 1T-b modes saturate at high sound speed because of the frequencies being lower than the cutoff frequency. Given the sound speed of 763 m/s, f_{p1} and f_{p2} from the experiments are close to 1L1T-a and 1L1T-b modes from the FEM, respectively. Therefore, the pressure distribution along the axial direction for these modes are compared in Fig. 11.

Figure 11 illustrates the pressure magnitude and phase distribution from the experiments and the FEM in axial direction for 1L1T-a and 1L1T-b modes. Notice that for 1L1T-a mode, a discrepancy between the experiments and the FEM appears, i.e., the nodal line location is not consistent, and the phase relationship between the sensors does not match. Specifically, sensor 1 is nearly in phase with sensor 2 and 3 in the experiments, which is not in the FEM. 1L1T-b mode from the FEM is relatively close to that from the experiment, but the optimal sound speed is supposed to provide a good agreement for both modes simultaneously. Therefore, one can conclude that not only is 794 m/s the optimal sound speed, but also estimating the sound speed by minimizing a least squares error is acceptable. Once the sound speed is determined, the associated temperature can be estimated from the ideal gas assumption, i.e., $c = \sqrt{\gamma \mathscr{R} T}$ where γ and $\mathscr{R}$ are specific heat ratio and the gas constant for air, respectively, under lean condition.